

Superconductivity in Te-deficient ZrTe_2

Lucas E. Correa,[†] Pedro P. Ferreira,^{*,†,‡} Leandro R. de Faria,[†] Vitor M. Fim,[†]
 Mario S. da Luz,[¶] Milton S. Torikachvili,[§] Christoph Heil,[‡] Luiz T. F. Eleno,[†]
 and Antonio J. S. Machado^{*,†}

[†]*Universidade de São Paulo, Escola de Engenharia de Lorena, DEMAR, 12612-550,
 Lorena, Brazil*

[‡]*Institute of Theoretical and Computational Physics, Graz University of Technology, NAWI
 Graz, 8010, Graz, Austria*

[¶]*Instituto de Ciências Tecnológicas e Exatas, Universidade Federal do Triângulo Mineiro,
 38025-180, Uberaba, Minas Gerais, Brazil*

[§]*Department of Physics, San Diego State University, San Diego, CA 92182-1233, USA*

E-mail: pedroferreira@usp.br; ajefferson@usp.br

Abstract

We present structural, electrical, and thermoelectric potential measurements on high-quality single crystals of $\text{ZrTe}_{1.8}$ grown from isothermal chemical vapor transport. These measurements show that the Te-deficient $\text{ZrTe}_{1.8}$, which forms the same structure as the non-superconducting ZrTe_2 , is superconducting below 3.2 K. The temperature dependence of the upper critical field (H_{c2}) deviates from the behavior expected in conventional single-band superconductors, being best described by an electron-phonon two-gap superconducting model with strong intraband coupling. For the $\text{ZrTe}_{1.8}$ single crystals, the Seebeck potential measurements suggest that the charge carriers are predominantly negative, in agreement with the ab initio calculations. Through first-principles calculations within DFT, we show that the slight reduction of Te occupancy

in ZrTe_2 unexpectedly gives origin to density of states peaks at the Fermi level due to the formation of localized Zr- d bands, possibly promoting electronic instabilities at the Fermi level and an increase at the critical temperature according to the standard BCS theory. These findings highlight that the Te deficiency promotes the electronic conditions for the stability of the superconducting ground state, suggesting that defects can fine-tune the electronic structure to support superconductivity.

Introduction

The transition metal dichalcogenides (TMDs), with chemical composition TX_2 , where $\text{T} = \text{Zr}, \text{Hf}, \text{Ti}, \text{Mo}, \text{W}, \text{Ta}, \text{etc.}$, and $\text{X} = \text{S}, \text{Se}, \text{Te}$, display a rich number of important physical properties and have the potential for many applications.^{1–11} These materials frequently crystallize in low-dimensional structures and exhibit coherent states and electronic instabilities, such as charge density waves (CDW) and superconductivity (SC).^{12–22} Their low-dimensional, layered structures are held together by weak van der Waals forces, and SC can emerge upon intercalation of different species in the interstices of the structural van der Waals gap.^{23–26} In addition to SC and CDW, recent studies suggest that many of these TMDs exhibit non-trivial topology, especially type-II topological Dirac states, increasing the interest in this class of materials.^{27–31}

The focus of this work is the ZrTe_{2-x} TMD, a Te-deficient compositional modification of the ZrTe_2 which crystallizes in the well-known CdI_2 -prototype structure $P\bar{3}m1$ (164),³² which is attracting intense attention of the physical chemistry research community.^{33–43} Ionic intercalation can be accomplished in ZrTe_2 by positioning the foreign species in the van der Waals gap, frequently leading to SC, e.g. Cu_xZrTe_2 ($T_c \approx 9.0 \text{ K}$) and Ni_xZrTe_2 ($T_c \approx 4.0 \text{ K}$).^{44,45} In the case of Ni_xZrTe_2 , for instance, the possible coexistence of multi-gap superconductivity and CDW ($T_{CDW} \approx 287 \text{ K}$) instabilities are well established. Additionally, recent angle-resolved photoemission spectroscopy and de Haas-van Alphen oscillations experiments also suggest that ZrTe_2 can be regarded as a Dirac semimetal with massless

4-fold quasiparticles.^{46,47} Due to the possible coexistence of SC and non-trivial topological properties, ZrTe_2 is an excellent candidate for probing the interplay between different emergent quantum states.

While the connection between intercalation and SC has been reported in ZrTe_2 ,^{44,45} the effect of slight compositional variations and defects has not been probed. Here we address the effect of Te deficiency on the electronic properties of ZrTe_2 , and we show that SC can emerge due to slight structural and electronic modifications. Vacancies at the Te sites are introduced in a controlled fashion using isothermal chemical vapor transport (ICVT) growth and the emergence of SC is characterized by means of electrical resistivity, AC susceptibility, and thermoelectric potential measurements. Our measurements suggest that $\text{ZrTe}_{1.8}$ is a two-gap superconductor below approximately 3.2 K with relatively strong intraband coupling. Furthermore, we calculated the band structure of $\text{ZrTe}_{1.75}$ within the density functional theory and supercell method. We found that the inclusion of vacancies in bulk ZrTe_2 gives rise to a peak at the density of states (DOS) at the Fermi level due to the formation of localized Zr-*d* bands, bridging the way to electronic instabilities at the Fermi surface.

Methods

Experimental details

The ZrTe_{2-x} single crystals were prepared by means of the isothermal chemical vapor transport (ICVT), recently proposed by some of the present authors.⁴⁸ Pre-reacted ZrTe_{2-x} pellets were synthesized by solid-state reaction, and they served as precursors for the ICVT growth. The pellets and a small amount of iodine, which serves as a transport agent, were sealed in a quartz tube, and the growth took place over seven days in temperatures at 950° C. As a result, the crystals grow out of the pellets, and the typical dimensions of the largest crystals are $10 \times 10 \times 0.1 \text{ mm}^3$. The growth details are discussed in Ref.⁴⁸

The composition was determined from energy dispersive spectroscopy (EDS) and induced

coupling plasma (ICP) utilizing microwave plasma atomic emission spectroscopy (MP-AES) after dilution in HNO_3 and HCl . For the MP-AES measurements, sample replicates, reagent blanks, and standard samples with precisely known compositions were used for cross-checking and ensuring accuracy. The crystallographic quality of crystals was verified by X-ray diffraction (XRD) using a Panalytical-Empryean diffractometer. Rocking curves centered on the $(00l)$ reflections were used to ascertain the orientation and level of crystallinity.

The electrical resistivity, AC susceptibility, and thermoelectric potential measurements were carried out with the Physical Property Measurement System PPMS-9 from Quantum Design, equipped with a 9.0 T superconducting magnet. For the 4-probe resistivity measurements, four copper leads were attached to the sample using silver paste. The typical contact resistance was in the $4\text{-}5\,\Omega$ range. The magnetization measurements were performed using the vibration sample magnetometer (VSM). The AC susceptibility measurements were carried out with the ACMS II option of the PPMS, with excitation fields of 1 and 2 Oe, in the frequency range from 1000-4000 Hz. The Seebeck coefficient was measured using the thermal transport option of the PPMS-9. The sample was placed across a small printed circuit board section containing four copper lines. Contact of the sample with the copper lines was established with Ni-loaded epoxy.

Computational methods

First-principles electronic-structure calculations were performed within the Kohn-Sham scheme⁴⁹ of the Density Functional Theory (DFT)⁵⁰ with scalar-relativistic optimized norm-conserving Vanderbilt pseudopotentials⁵¹ as implemented in Quantum Espresso.^{52,53} Exchange and Correlation (XC) effects were treated with the generalized gradient approximation (GGA) according to vdW-DF2-C09 parametrization,^{54,55} explicitly including the non-local van der Waals interactions. All numerical parameters were exhaustively tested to guarantee a total energy convergence lower than 3 meV/atom. Based on the convergence results, we adopted a kinetic energy cutoff of 60 Ry for the wave functions and 240 Ry for the charge density and

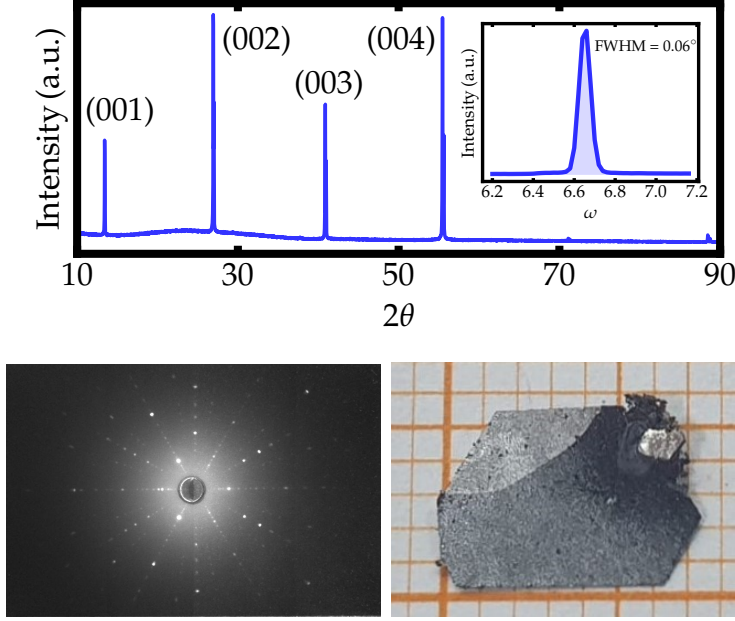


Figure 1: θ - 2θ XRD scan of the $\text{ZrTe}_{1.8}$ crystal with beam incident on the flat surface (ab -plane). The inset shows the rocking curve centered on the (001) reflection. The lower panel shows the Laue patterns of the $\text{ZrTe}_{1.8}$ reciprocal lattice (left) and the picture of one representative single crystal with dimensions $6.5 \times 5.5 \times 0.1 \text{ mm}^3$ (right).

potential, and a centered $4 \times 4 \times 4$ k -point sampling in the first Brillouin according to the Monkhorst-Pack scheme.⁵⁶ A denser $24 \times 24 \times 24$ k -point grid was used to obtain the DOS. Self-consistent-field calculations were carried out using the Methfessel-Paxton smearing⁵⁷ with a spreading of 0.005 Ry for Brillouin-zone integration, while the optimized tetrahedron method⁵⁸ was adopted for the electronic occupation in non-self-consistent-field calculations. All lattice parameters and internal degrees of freedom were relaxed to achieve a ground-state convergence of 10^{-7} Ry in total energy and 10^{-6} Ry/ a_0 for forces acting on the nuclei. The convergence criteria for self-consistency adopted was 10^{-10} Ry. The supercells were generated with the supercell code.⁵⁹

Results and discussion

We synthesized single crystals from a precursor with nominal composition $\text{ZrTe}_{1.8}$. The EDS and ICP elemental analysis indicated $\text{ZrTe}_{1.8}$ and $\text{ZrTe}_{1.85}$ compositions, respectively.

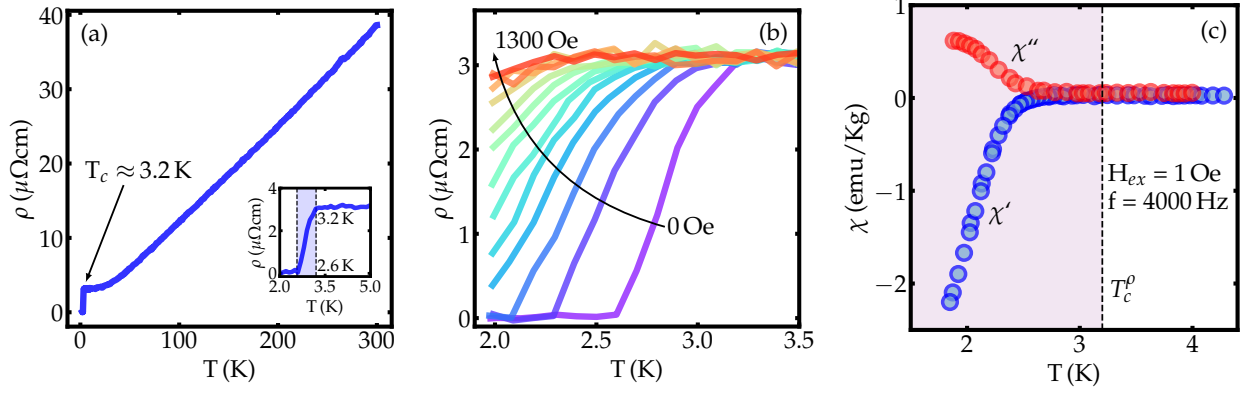


Figure 2: (a) Temperature dependence of the electrical resistivity for the $\text{ZrTe}_{1.8}$. The inset presents the low-temperature region, showing the onset of the SC transition near 3.2 K and the completion at 2.6 K. (b) Effect of magnetic fields up to 1300 Oe on the resistive transition to SC. c) AC magnetic susceptibility χ versus temperature for an applied magnetic field of 1 Oe and frequency 4000 Hz.

For simplicity, heretofore, we will refer to the $\text{ZrTe}_{1.8}$ composition. A θ - 2θ XRD scan with the incident beam on the flat surface of a crystal (ab -plane) is displayed in Fig. 1. It only shows $(00l)$ reflections, which suggests that flat faces are the basal plane of the trigonal CdI_2 structure. The XRD scan is consistent with the Zr–Te phase diagram,⁶⁰ where the $P\bar{3}m1$ space group was experimentally determined to be stable in a wide composition range, i.e., ZrTe_{2-x} ($x = 0\text{--}0.28$). The inset of Fig. 1 shows the rocking curve centered on the (001) reflection. This reflection is centered at $\theta = 6.66^\circ$, and the full width at half maximum (FWHM) is $\approx 0.06^\circ$. The narrow FWHM is consistent with excellent crystallinity. The Te deficient crystals had a dull silvery appearance and typical sizes of $6 \times 6 \times 0.05 \text{ mm}^3$, as shown in Fig. 1.

The temperature dependence of the electrical resistivity of the $\text{ZrTe}_{1.8}$ is shown in Fig. 2(a). The resistivity drops nearly linearly upon cooling from 300 K, it starts leveling off around 40 K, and eventually drops to zero with the onset of SC at $T_c \approx 3.2 \text{ K}$. Fig. 2(b) shows the effect of the magnetic field on the resistive transition to SC in fields up to 1300 Oe. The shift of the 3.2 K transition to lower temperature as a function of the applied magnetic field is consistent with SC. Further support for bulk superconductivity is provided by the AC

magnetic susceptibility χ near T_c , as shown in Fig. 2c, for data collected with an excitation field $H_{ex} = 1$ Oe and frequency $f = 4000$ Hz. While in-phase component χ' reveals a large diamagnetic signal below T_c , the out-of-phase component χ'' increases, reflecting the dissipation associated with the onset of flux dynamics.

Using the magneto-resistance data of Fig. 2 and taking T_c from the onset of the superconducting transitions, the upper critical field H_{c2} can be plotted as a function of the reduced temperature $t = T/T_c$, as shown in Fig. 3. The $H_{c2}(T)$ data show an upturn below

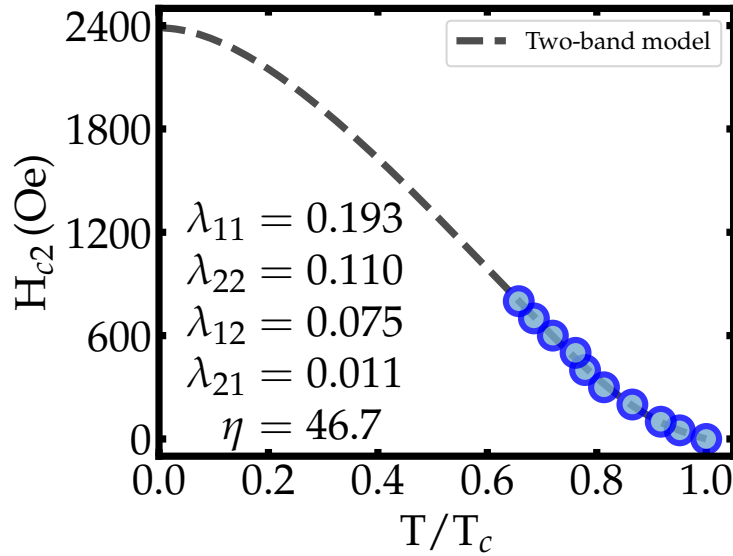


Figure 3: Upper critical magnetic field H_{c2} vs reduced temperature T/T_c . The values of H_{c2} were taken from the onset of the resistive transitions. The dashed line is a fit to the data using Gurevich's two-band model.

T_c , in sharp contrast with the expected quadratic behavior of single-band superconductivity and the Werthamer-Helfand-Hohenberg (WHH) single-gap model.⁶¹ The positive curvature of H_{c2} below T_c is frequently taken as an indication of multi-band SC.⁶²⁻⁶⁷ Alternatively, the fit of the $H_{c2}(T)$ data to the two-band model proposed by Gurevich⁶⁸ results in an excellent fit, as seen in Fig. 3, where is represented by the dashed black line. In Gurevich's model,⁶⁸

the equation for H_{c2} takes the form

$$\begin{aligned} a_0 [\log t + U(h)] [\log t + U(\eta h)] + a_1 [\log t + U(h)] \\ + a_2 [\log t + U(\eta h)] = 0, \end{aligned} \quad (1)$$

where $a_0 = 2w/\lambda_0$, $a_1 = 1 + \lambda_-/\lambda_0$, and $a_2 = 1 - \lambda_-/\lambda_0$, with $\lambda_- = \lambda_{11} - \lambda_{22}$, $w = \lambda_{11}\lambda_{22} - \lambda_{12}\lambda_{21}$, and $\lambda_0 = (\lambda_-^2 + 4\lambda_{12}\lambda_{21})^2$. The coefficients λ_{mn} are the eigenvalues of the BCS superconducting coupling matrix. The diagonal terms λ_{11} and λ_{22} quantify the intraband coupling, whereas the off-diagonal terms λ_{12} and λ_{21} describe the interband coupling. The function $U(x)$ is defined as $U(x) = \psi(1/2+x) - \psi(1/2)$, where $\psi(x)$ is the di-gamma function. The arguments of the $U(x)$ in Eq. 1 are given by $h = H_{c2}D_1/2\phi_0T$ and $\eta = D_1/D_2$, where D_1 and D_2 are the intraband electronic diffusivities of bands 1 and 2 in the normal state, and ϕ_0 is the magnetic flux quanta. The derivation of the intraband diffusivity tensors $D_m^{\alpha\beta}$ expressed in terms of microscopic parameters can be found in Appendix A of the Ref.⁶⁸

The fit to the two-band model yields a $H_{c2}(0)$ value of ≈ 2400 Oe, which is consistent with the trend from the H_{c2} data extracted from the resistivity measurements. The diffusivity and coupling parameters yielded by the two-band fit are $\lambda_{11} = 0.193$ and $\lambda_{22} = 0.110$ (intraband coupling), $\lambda_{12} = 0.075$ and $\lambda_{21} = 0.011$ (interband coupling), and $\eta = 46.7$. The high diffusivity ratio η reflects the significant difference between the electron mobility of distinct Fermi Surface sheets involved in the pairing mechanism, which originates the positive curvature of $H_{c2}(T)$. Still, the λ_{mn} values extracted from the effective model suggest that the intraband coupling is one order of magnitude higher than the interband scattering, which likely is the main driving force for the multi-band-type behavior observed. Consistently, SC in ZrTe₂ intercalated with Ni and Cu has also been linked to multi-band behavior.^{44,45} Given that SC in Te-deficient ZrTe_{1.8} is also consistent with multi-band behavior, we propose that the multi-gap SC state often observed in intercalated TMDs is not necessarily related to the intercalation, but rather it is intrinsically related to the TMDs electronic structure.

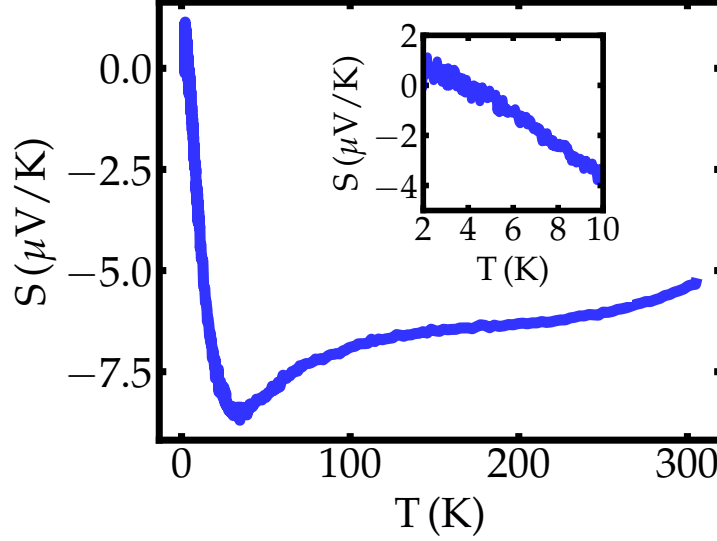


Figure 4: Seebeck coefficient as a function of temperature for $\text{ZrTe}_{1.8}$.

Measurements of the thermoelectric potential (Fig. 4) suggest that the preponderance of charge carriers are electrons. The Seebeck potential is $\approx -5.2 \mu\text{V/K}$ near ambient temperature. It becomes slightly more negative upon cooling, reaching at minimum ($\approx -8.5 \mu\text{V/K}$) near 35 K, and increasing rapidly below 20 K, reaching zero value near T_c , consistent with SC pairing. The complex behavior of $S(T)$ near 35 K possibly results from the convoluted interplay between the temperature dependence of the electron concentration, the asymmetry of the electron distribution near the Fermi level, the mean free path, and mean scattering time. To the best of our knowledge, this is the first time that bulk SC was observed in ZrTe_2 , albeit Te-deficient, without intercalation or pressure. The emergence of SC in Te-deficient ZrTe_2 suggests that the Te vacancies or the resulting crystalline defects play a crucial role, and a better understanding is still in order.

Ab initio assessment

To probe the effects of tellurium defects, we generated $2 \times 2 \times 2$ supercells by occupying 85 % of the two non-equivalent Te atomic sites within the $2d$ Wyckoff position of the unit cell.

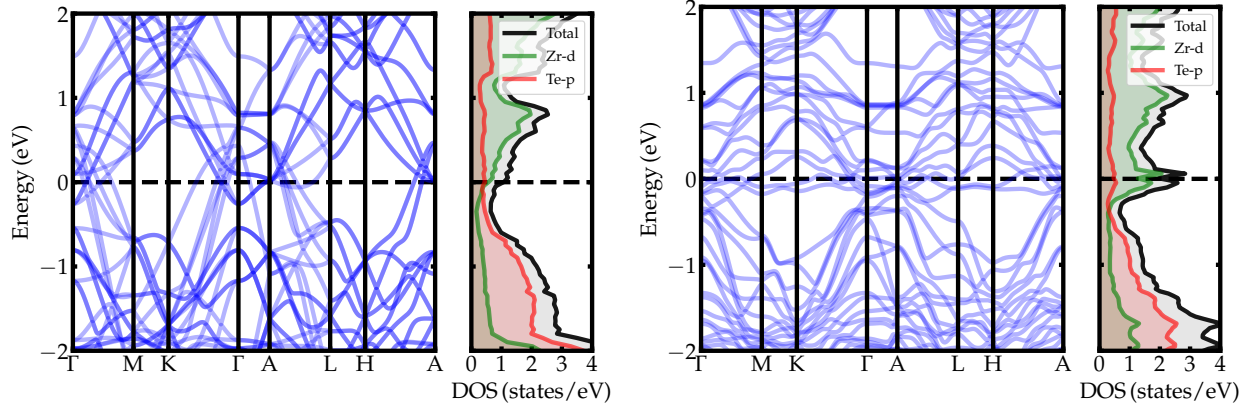


Figure 5: (left) Electronic band structure and DOS for pure ZrTe_2 in a $2 \times 2 \times 2$ supercell. (right) Electronic band structure for the cluster with the lowest formation energy and averaged DOS for $\text{ZrTe}_{1.75}$ in a $2 \times 2 \times 2$ supercell. The averaged DOS was weighted according to the degeneracy of each non-equivalent structural configuration.

With that, there are 64 possible structural configurations, which we can reduce to only four unique clusters (with different multiplicities) by identifying and employing the full symmetry operations of each supercell.

Figure 5 shows the electronic structure for the pure $2 \times 2 \times 2$ ZrTe_2 supercell and the averaged Te-deficient supercell with composition $\text{ZrTe}_{1.75}$ weighted according to the cluster degeneracies. The total DOS at the Fermi level for pure ZrTe_2 is 1.1 states/eV. This value is consistent with previous calculations, which include the spin-orbit coupling,⁴⁵ yielding 1.0 states/eV at the Fermi level, a percentage difference of only 8% with respect to our results without including spin-orbit coupling. From the 1.1 states/eV, approximately 53% originate from the Zr-*d* electron pockets, whereas 42% are coming from the Te-*p* hole pockets. With the inclusion of Te vacancies, a narrow DOS peak at the Fermi level develops due to the formation of localized, near-flat Zr-*d* electronic bands along the entire extent of the Brillouin zone. The averaged $\text{ZrTe}_{1.75}$ has 2.1 states/eV at the Fermi level, an increase of 92% compared to pure ZrTe_2 , of which approximately 65% are derived from the Zr-*d* orbitals, and only 23% are coming from the Te-*p* orbitals. Since most of the Zr-*d* states are electron-like pockets at the Fermi surface, the increase of the Zr-*d* character at the Fermi level is consistent with the polarity of the Seebeck potential determined experimentally, revealing

that the charge carriers are predominantly negative.

According to the BCS theory, the electronic states that contribute the most to SC are those with energies within a range of the order of $\hbar\omega_D$ around the Fermi energy, where ω_D is the Debye frequency, and, assuming that the DOS within the energy range $\hbar\omega_D$ is constant, the superconducting critical temperature follows the relation $T_c \approx \hbar\omega_D \exp[-1/N(\epsilon)\lambda]$, where λ is the electron-phonon coupling strength.⁶⁹ Therefore, the increased DOS at the Fermi level due to the formation of Te vacancies leads to a significant increase in the critical temperature, explaining the relatively high critical temperature in $\text{ZrTe}_{1.8}$ compared to the non-superconducting defect-free compound. Furthermore, the Te vacancies also give rise to a sharp DOS peak at E_F , similar to van Hove-type singularities, i.e., the DOS varies rapidly within the $\hbar\omega_D$ energy range. When electron correlation effects are considered, this logarithmic instability also enhances T_c and favors spontaneous symmetry-breaking phase transitions.^{70–75} Therefore, the appearance of localized states near the Fermi level and the substantial increase of the total DOS at E_F reasonably explains on qualitative grounds the defect-induced SC in ZrTe_2 .

In order to describe the superconducting state observed in $\text{ZrTe}_{1.8}$, one would need to employ advanced techniques such as the fully anisotropic Migdal-Eliashberg theory⁷⁶ or Superconducting Density Functional Theory^{77–79} to accurately take into account the anisotropy of the electron-phonon coupling and the two-gap feature of the superconducting gap function. As the presence of Te vacancies necessitates the consideration of supercells and very dense samplings of the Brillouin zone are required to obtain convergence, such a calculation is beyond the scope of the current work, but will be the focus of a future project.

Conclusions

This work shows the emergence of superconductivity in $\text{ZrTe}_{1.8}$, a Te-deficient, off-stoichiometry composition of the non-superconducting TMD ZrTe_2 , on high-quality single crystals synthe-

sized by ICVT. The superconducting properties were characterized by measurements of electrical resistivity, AC susceptibility, and thermoelectric potential. The $\text{ZrTe}_{1.8}$ composition gives rise to a multi-gap superconducting state with a critical temperature close to 3.2 K. Interestingly, the presence of DOS peak at the Fermi level due to localized Zr- d bands can be linked to the superconducting pairing in the Te-deficient ZrTe_2 . These results strongly suggest that native point defects, such as vacancies, are essential for SC in the widely investigated class of transition metal dichalcogenides. Furthermore, we show that the multi-band nature is intrinsic to ZrTe_2 and that these findings are possibly extending to the whole family of TMDs.

Acknowledgement

LEC, PPF, LTFE, and AJSM gratefully acknowledge the São Paulo Research Foundation (FAPESP) under Grants 2018/08819-2, 2019/17878-5, 2019/14359-7, 2020/08258-0, 2021/13441-1, 2021/14322-6. CH acknowledges the Austrian Science Fund (FWF) Project No. P 32144-N36. This study was supported by the Coordenação de Aperfeiçoamento de Pessoal de Nível Superior (CAPES) - Brasil - Finance Code 001, and was conducted by using computational resources of the dCluster of the Graz University of Technology, the VSC-5 of the Vienna University of Technology, and the SDumont supercomputer of the National Laboratory for Scientific Computing (LNCC/MCTI, Brazil).

References

- (1) Xu, X.; Yao, W.; Xiao, D.; Heinz, T. F. Spin and pseudospins in layered transition metal dichalcogenides. *Nature Physics* **2014**, *10*, 343–350.
- (2) Voiry, D.; Mohite, A.; Chhowalla, M. Phase engineering of transition metal dichalcogenides. *Chemical Society Reviews* **2015**, *44*, 2702–2712.

- (3) Kalantar-zadeh, K.; Ou, J. Z.; Daeneke, T.; Strano, M. S.; Pumera, M.; Gras, S. L. Two-dimensional transition metal dichalcogenides in biosystems. *Advanced Functional Materials* **2015**, *25*, 5086–5099.
- (4) Tedstone, A. A.; Lewis, D. J.; O’Brien, P. Synthesis, properties, and applications of transition metal-doped layered transition metal dichalcogenides. *Chemistry of Materials* **2016**, *28*, 1965–1974.
- (5) Choi, W.; Choudhary, N.; Han, G. H.; Park, J.; Akinwande, D.; Lee, Y. H. Recent development of two-dimensional transition metal dichalcogenides and their applications. *Materials Today* **2017**, *20*, 116–130.
- (6) Manzeli, S.; Ovchinnikov, D.; Pasquier, D.; Yazyev, O. V.; Kis, A. 2D transition metal dichalcogenides. *Nature Reviews Materials* **2017**, *2*, 1–15.
- (7) Han, G. H.; Duong, D. L.; Keum, D. H.; Yun, S. J.; Lee, Y. H. van der Waals metallic transition metal dichalcogenides. *Chemical reviews* **2018**, *118*, 6297–6336.
- (8) Liu, Y.; Gao, Y.; Zhang, S.; He, J.; Yu, J.; Liu, Z. Valleytronics in transition metal dichalcogenides materials. *Nano Research* **2019**, *12*, 2695–2711.
- (9) Zhang, X.; Teng, S. Y.; Loy, A. C. M.; How, B. S.; Leong, W. D.; Tao, X. Transition metal dichalcogenides for the application of pollution reduction: A review. *Nanomaterials* **2020**, *10*, 1012.
- (10) Wang, Z.; Li, R.; Su, C.; Loh, K. P. Intercalated phases of transition metal dichalcogenides. *SmartMat* **2020**, *1*, e1013.
- (11) Fu, Q.; Han, J.; Wang, X.; Xu, P.; Yao, T.; Zhong, J.; Zhong, W.; Liu, S.; Gao, T.; Zhang, Z., et al. 2D transition metal dichalcogenides: Design, modulation, and challenges in electrocatalysis. *Advanced Materials* **2021**, *33*, 1907818.

- (12) Klemm, R. A. Pristine and intercalated transition metal dichalcogenide superconductors. *Physica C: Superconductivity and its Applications* **2015**, *514*, 86–94.
- (13) Shi, W.; Ye, J.; Zhang, Y.; Suzuki, R.; Yoshida, M.; Miyazaki, J.; Inoue, N.; Saito, Y.; Iwasa, Y. Superconductivity series in transition metal dichalcogenides by ionic gating. *Scientific reports* **2015**, *5*, 1–10.
- (14) Rossnagel, K. On the origin of charge-density waves in select layered transition-metal dichalcogenides. *Journal of Physics: Condensed Matter* **2011**, *23*, 213001.
- (15) Zhu, X.; Guo, J.; Zhang, J.; Plummer, E. Misconceptions associated with the origin of charge density waves. *Advances in Physics: X* **2017**, *2*, 622–640.
- (16) Hsu, Y.-T.; Vaezi, A.; Fischer, M. H.; Kim, E.-A. Topological superconductivity in monolayer transition metal dichalcogenides. *Nature communications* **2017**, *8*, 1–6.
- (17) Heil, C.; Poncé, S.; Lambert, H.; Schlipf, M.; Margine, E. R.; Giustino, F. Origin of superconductivity and latent charge density wave in NbS₂. *Physical review letters* **2017**, *119*, 087003.
- (18) Ying, J.; Paudyal, H.; Heil, C.; Chen, X.-J.; Struzhkin, V. V.; Margine, E. R. Unusual pressure-induced periodic lattice distortion in SnSe₂. *Physical review letters* **2018**, *121*, 027003.
- (19) Lian, C.-S.; Heil, C.; Liu, X.; Si, C.; Giustino, F.; Duan, W. Coexistence of superconductivity with enhanced charge density wave order in the two-dimensional limit of TaSe₂. *The Journal of Physical Chemistry Letters* **2019**, *10*, 4076–4081.
- (20) Balandin, A. A.; Zaitsev-Zotov, S. V.; Grüner, G. Charge-density-wave quantum materials and devices—New developments and future prospects. *Applied Physics Letters* **2021**, *119*, 170401.

- (21) Xu, Z.; Yang, H.; Song, X.; Chen, Y.; Yang, H.; Liu, M.; Huang, Z.; Zhang, Q.; Sun, J.; Liu, L., et al. Topical review: recent progress of charge density waves in 2D transition metal dichalcogenide-based heterojunctions and their applications. *Nanotechnology* **2021**, *32*, 492001.
- (22) Lian, C.-S.; Heil, C.; Liu, X.; Si, C.; Giustino, F.; Duan, W. Intrinsic and doping-enhanced superconductivity in monolayer 1H-TaS₂: Critical role of charge ordering and spin-orbit coupling. *Physical Review B* **2022**, *105*, L180505.
- (23) Morosan, E.; Zandbergen, H. W.; Dennis, B.; Bos, J.; Onose, Y.; Klimczuk, T.; Ramirez, A.; Ong, N.; Cava, R. J. Superconductivity in Cu_xTiSe₂. *Nature Physics* **2006**, *2*, 544–550.
- (24) de Lima, B.; de Cassia, R.; Santos, F.; Correa, L.; Grant, T.; Manesco, A.; Martins, G.; Eleno, L.; Torikachvili, M.; Machado, A. Properties and superconductivity in Ti-doped NiTe₂ single crystals. *Solid State Communications* **2018**, *283*, 27–31.
- (25) Dutta, U.; Malavi, P.; Sahoo, S.; Joseph, B.; Karmakar, S. Pressure-induced superconductivity in semimetallic 1T-TiTe₂ and its persistence upon decompression. *Physical Review B* **2018**, *97*, 060503.
- (26) Sahoo, S.; Dutta, U.; Harnagea, L.; Sood, A.; Karmakar, S. Pressure-induced suppression of charge density wave and emergence of superconductivity in 1T-VSe₂. *Physical Review B* **2020**, *101*, 014514.
- (27) Belopolski, I.; Xu, S.-Y.; Ishida, Y.; Pan, X.; Yu, P.; Sanchez, D. S.; Zheng, H.; Neupane, M.; Alidoust, N.; Chang, G., et al. Fermi arc electronic structure and Chern numbers in the type-II Weyl semimetal candidate Mo_xW_{1-x}Te₂. *Physical Review B* **2016**, *94*, 085127.
- (28) Bahramy, M.; Clark, O.; Yang, B.-J.; Feng, J.; Bawden, L.; Riley, J.; Marković, I.; Mazola, F.; Sunko, V.; Biswas, D., et al. Ubiquitous formation of bulk Dirac cones and

- topological surface states from a single orbital manifold in transition-metal dichalcogenides. *Nature materials* **2018**, *17*, 21–28.
- (29) Fei, F.; Bo, X.; Wang, R.; Wu, B.; Jiang, J.; Fu, D.; Gao, M.; Zheng, H.; Chen, Y.; Wang, X., et al. Nontrivial Berry phase and type-II Dirac transport in the layered material PdTe₂. *Physical Review B* **2017**, *96*, 041201.
- (30) Ferreira, P. P.; Manesco, A. L.; Dorini, T. T.; Correa, L. E.; Weber, G.; Machado, A. J.; Eleno, L. T. Strain engineering the topological type-II Dirac semimetal NiTe₂. *Physical Review B* **2021**, *103*, 125134.
- (31) Kar, I.; Chatterjee, J.; Harnagea, L.; Kushnirenko, Y.; Fedorov, A.; Shrivastava, D.; Büchner, B.; Mahadevan, P.; Thirupathaiah, S. Metal-chalcogen bond-length induced electronic phase transition from semiconductor to topological semimetal in ZrX₂ (X = Se and Te). *Physical Review B* **2020**, *101*, 165122.
- (32) Jobic, S.; Brec, R.; Rouxel, J. Anionic polymeric bonds in transition metal ditellurides. *Journal of Solid State Chemistry* **1992**, *96*, 169–180.
- (33) Zhuang, H. L.; Hennig, R. G. Computational search for single-layer transition-metal dichalcogenide photocatalysts. *The Journal of Physical Chemistry C* **2013**, *117*, 20440–20445.
- (34) Guo, H.; Lu, N.; Wang, L.; Wu, X.; Zeng, X. C. Tuning electronic and magnetic properties of early transition-metal dichalcogenides via tensile strain. *The Journal of Physical Chemistry C* **2014**, *118*, 7242–7249.
- (35) Rasmussen, F. A.; Thygesen, K. S. Computational 2D materials database: electronic structure of transition-metal dichalcogenides and oxides. *The Journal of Physical Chemistry C* **2015**, *119*, 13169–13183.

- (36) Alyoruk, M. M.; Aierken, Y.; Cakir, D.; Peeters, F. M.; Sevik, C. Promising piezoelectric performance of single layer transition-metal dichalcogenides and dioxides. *The Journal of Physical Chemistry C* **2015**, *119*, 23231–23237.
- (37) Lee, J.; Kang, S.; Yim, K.; Kim, K. Y.; Jang, H. W.; Kang, Y.; Han, S. Hydrogen evolution reaction at anion vacancy of two-dimensional transition-metal dichalcogenides: ab initio computational screening. *The Journal of Physical Chemistry Letters* **2018**, *9*, 2049–2055.
- (38) Wang, H.; Chan, C. H.; Suen, C. H.; Lau, S. P.; Dai, J.-Y. Magnetotransport properties of layered topological material ZrTe₂ thin film. *ACS Nano* **2019**, *13*, 6008–6016.
- (39) Muhammad, Z.; Zhang, B.; Lv, H.; Shan, H.; Rehman, Z. U.; Chen, S.; Sun, Z.; Wu, X.; Zhao, A.; Song, L. Transition from semimetal to semiconductor in ZrTe₂ induced by Se substitution. *ACS Nano* **2019**, *14*, 835–841.
- (40) Ng, S. M.; Wang, H.; Liu, Y.; Wong, H. F.; Yau, H. M.; Suen, C. H.; Wu, Z. H.; Leung, C. W.; Dai, J.-Y. High-temperature anomalous Hall effect in a transition metal dichalcogenide ferromagnetic insulator heterostructure. *ACS Nano* **2020**, *14*, 7077–7084.
- (41) Zhang, B.; Muhammad, Z.; Wang, P.; Cui, S.; Li, Y.; Wang, S.; Wu, Y.; Liu, Z.; Zhu, H.; Liu, Y., et al. Electronic structures of cr-intercalated ZrTe₂ revealed by angle-resolved photoemission spectroscopy. *The Journal of Physical Chemistry C* **2020**, *124*, 16561–16567.
- (42) Villaos, R. A. B.; Cruzado, H. N.; Dizon, J. S. C.; Maghirang III, A. B.; Huang, Z.-Q.; Hsu, C.-H.; Huang, S.-M.; Lin, H.; Chuang, F.-C. Evolution of the electronic properties of ZrX₂ (X= S, Se, or Te) thin films under varying thickness. *The Journal of Physical Chemistry C* **2021**, *125*, 1134–1142.

- (43) Ren, M.-Q.; Han, S.; Fan, J.-Q.; Wang, L.; Wang, P.; Ren, W.; Peng, K.; Li, S.; Wang, S.-Z.; Zheng, F.-W., et al. Semiconductor–Metal Phase Transition and Emergent Charge Density Waves in 1 T-ZrX₂ (X= Se, Te) at the Two-Dimensional Limit. *Nano Letters* **2022**, *22*, 476–484.
- (44) Machado, A.; Baptista, N.; De Lima, B.; Chaia, N.; Grant, T.; Corrêa, L.; Renosto, S.; Scaramussa, A.; Jardim, R.; Torikachvili, M., et al. Evidence for topological behavior in superconducting Cu_xZrTe_{2-y}. *Physical Review B* **2017**, *95*, 144505.
- (45) Correa, L. E.; Ferreira, P. P.; de Faria, L. R.; Dorini, T. T.; da Luz, M. S.; Fisk, Z.; Torikachvili, M. S.; Eleno, L. T.; Machado, A. J. Evidence for multiband superconductivity and charge density waves in Ni-doped ZrTe₂. *Journal of Alloys and Compounds* **2022**, *907*, 164477.
- (46) Tsipas, P.; Tsoutsou, D.; Fragkos, S.; Sant, R.; Alvarez, C.; Okuno, H.; Renaud, G.; Alcotte, R.; Baron, T.; Dimoulas, A. Massless dirac fermions in ZrTe₂ semimetal grown on InAs (111) by van der Waals epitaxy. *ACS nano* **2018**, *12*, 1696–1703.
- (47) Nguyen, T.; Aryal, N.; Pokharel, B. K.; Harnagea, L.; Mierstchin, D.; Popović, D.; Graf, D.; Shrestha, K. Fermiology of the Dirac type-II semimetal candidates (Ni, Zr) Te₂ using de Haas–van Alphen oscillations. *Physical Review B* **2022**, *106*, 075154.
- (48) Correa, L. E.; de Faria, L. R.; Cardoso, R. S.; Chaia, N.; da Luz, M. S.; Torikachvili, M. S.; Machado, A. J. Growth of pure and intercalated ZrTe₂, TiTe₂ and HfTe₂ dichalcogenide single crystals by isothermal chemical vapor transport. *Journal of Crystal Growth* **2022**, *595*, 126819.
- (49) Kohn, W.; Sham, L. J. Self-consistent equations including exchange and correlation effects. *Physical review* **1965**, *140*, A1133.
- (50) Hohenberg, P.; Kohn, W. Inhomogeneous electron gas. *Physical review* **1964**, *136*, B864.

- (51) Hamann, D. Optimized norm-conserving Vanderbilt pseudopotentials. *Physical Review B* **2013**, *88*, 085117.
- (52) Giannozzi, P.; Baroni, S.; Bonini, N.; Calandra, M.; Car, R.; Cavazzoni, C.; Ceresoli, D.; Chiarotti, G. L.; Cococcioni, M.; Dabo, I., et al. QUANTUM ESPRESSO: a modular and open-source software project for quantum simulations of materials. *Journal of physics: Condensed matter* **2009**, *21*, 395502.
- (53) Giannozzi, P.; Andreussi, O.; Brumme, T.; Bunau, O.; Nardelli, M. B.; Calandra, M.; Car, R.; Cavazzoni, C.; Ceresoli, D.; Cococcioni, M., et al. Advanced capabilities for materials modelling with Quantum ESPRESSO. *Journal of physics: Condensed matter* **2017**, *29*, 465901.
- (54) Lee, K.; Murray, É. D.; Kong, L.; Lundqvist, B. I.; Langreth, D. C. Higher-accuracy van der Waals density functional. *Physical Review B* **2010**, *82*, 081101.
- (55) Cooper, V. R. Van der Waals density functional: An appropriate exchange functional. *Physical Review B* **2010**, *81*, 161104.
- (56) Monkhorst, H. J.; Pack, J. D. Special points for Brillouin-zone integrations. *Physical review B* **1976**, *13*, 5188.
- (57) Methfessel, M.; Paxton, A. High-precision sampling for Brillouin-zone integration in metals. *Physical Review B* **1989**, *40*, 3616.
- (58) Kawamura, M.; Gohda, Y.; Tsuneyuki, S. Improved tetrahedron method for the Brillouin-zone integration applicable to response functions. *Physical Review B* **2014**, *89*, 094515.
- (59) Okhotnikov, K.; Charpentier, T.; Cadars, S. Supercell program: a combinatorial structure-generation approach for the local-level modeling of atomic substitutions and partial occupancies in crystals. *Journal of cheminformatics* **2016**, *8*, 1–15.

- (60) Okamoto, H. Te-Zr (tellurium-zirconium). *Journal of phase equilibria* **1999**, *20*.
- (61) Werthamer, N.; Helfand, E.; Hohenberg, P. Temperature and purity dependence of the superconducting critical field, H_{c2} . III. Electron spin and spin-orbit effects. *Physical Review* **1966**, *147*, 295.
- (62) Lyard, L.; Samuely, P.; Szabo, P.; Klein, T.; Marcenat, C.; Paulius, L.; Kim, K.; Jung, C.; Lee, H.-S.; Kang, B., et al. Anisotropy of the upper critical field and critical current in single crystal MgB_2 . *Physical Review B* **2002**, *66*, 180502.
- (63) Hunte, F.; Jaroszynski, J.; Gurevich, A.; Larbalestier, D.; Jin, R.; Sefat, A.; McGuire, M. A.; Sales, B. C.; Christen, D. K.; Mandrus, D. Two-band superconductivity in $\text{LaFeAsO}_{0.89}\text{F}_{0.11}$ at very high magnetic fields. *Nature* **2008**, *453*, 903–905.
- (64) Lei, H.; Graf, D.; Hu, R.; Ryu, H.; Choi, E.; Tozer, S.; Petrovic, C., et al. Multiband effects on β -FeSe single crystals. *Physical Review B* **2012**, *85*, 094515.
- (65) Xu, C.; Li, B.; Feng, J.; Jiao, W.; Li, Y.; Liu, S.; Zhou, Y.; Sankar, R.; Zhigadlo, N. D.; Wang, H., et al. Two-gap superconductivity and topological surface states in TaOsSi . *Physical Review B* **2019**, *100*, 134503.
- (66) Bhattacharyya, A.; Ferreira, P.; Santos, F.; Adroja, D.; Lord, J.; Correa, L.; Machado, A. J. d. S.; Manesco, A. L.; Eleno, L. T. Two-band superconductivity with unconventional pairing symmetry in HfV_2Ga_4 . *Physical Review Research* **2020**, *2*, 022001.
- (67) De Faria, L. R.; Ferreira, P. P.; Correa, L. E.; Eleno, L. T.; Torikachvili, M. S.; Machado, A. J. Possible multiband superconductivity in the quaternary carbide YRe_2SiC . *Superconductor Science and Technology* **2021**, *34*, 065010.
- (68) Gurevich, A. Enhancement of the upper critical field by nonmagnetic impurities in dirty two-gap superconductors. *Physical Review B* **2003**, *67*, 184515.

- (69) Annett, J. F., et al. *Superconductivity, superfluids and condensates*; Oxford University Press, 2004; Vol. 5.
- (70) Lie, S.; Carbotte, J. Dependence of T_c on electronic density of states. *Solid State Communications* **1978**, *26*, 511–514.
- (71) Pickett, W. E. Generalization of the theory of the electron-phonon interaction: Thermodynamic formulation of superconducting-and normal-state properties. *Physical Review B* **1982**, *26*, 1186.
- (72) Mitrović, B.; Carbotte, J. Effects of energy dependence in the electronic density of states on some normal state properties. *Canadian journal of physics* **1983**, *61*, 758–783.
- (73) Newns, D.; Pattnaik, P.; Tsuei, C. Role of Van Hove singularity in high-temperature superconductors: Mean field. *Physical Review B* **1991**, *43*, 3075.
- (74) Sano, W.; Koretsune, T.; Tadano, T.; Akashi, R.; Arita, R. Effect of Van Hove singularities on high- T_c superconductivity in H_3S . *Physical Review B* **2016**, *93*, 094525.
- (75) Chen, X.-J. Exploring high-temperature superconductivity in hard matter close to structural instability. *Matter and Radiation at Extremes* **2020**, *5*, 068102.
- (76) Margine, E. R.; Giustino, F. Anisotropic Migdal-Eliashberg theory using wannier functions. *Physical Review B* **2013**, *87*, 024505.
- (77) Oliveira, L. N. d.; Gross, E.; Kohn, W. Density-functional theory for superconductors. *Physical Review Letters* **1988**, *60*, 2430.
- (78) Lüders, M.; Marques, M.; Lathiotakis, N.; Floris, A.; Profeta, G.; Fast, L.; Continenza, A.; Massidda, S.; Gross, E. Ab initio theory of superconductivity. I. Density functional formalism and approximate functionals. *Physical Review B* **2005**, *72*, 024545.

- (79) Marques, M.; Lüders, M.; Lathiotakis, N.; Profeta, G.; Floris, A.; Fast, L.; Continenza, A.; Gross, E.; Massidda, S. Ab initio theory of superconductivity. II. Application to elemental metals. *Physical Review B* **2005**, *72*, 024546.

Graphical TOC Entry

